machines

MDPI

Article

Design and Characterization of a Rolling-Contact Involute Joint and Its Applications in Finger Exoskeletons

Renghao Liang [1], Guanghua Xu [1,2,*], Qiuxiang Zhang [1], Kaiyuan Jiang [1], Min Li [1] and Bo He [1]

[1] School of Mechanical Engineering, Xi'an Jiaotong University, Xi'an 710049, China; lrh8131@stu.xjtu.edu.cn (R.L.); zhangqx@stu.xjtu.edu.cn (Q.Z.); jiangkaiyuan98@stu.xjtu.edu.cn (K.J.); min.li@mail.xjtu.edu.cn (M.L.); xajthx@stu.xjtu.edu.cn (B.H.)
[2] State Key Laboratory for Manufacturing Systems Engineering, Xi'an Jiaotong University, Xi'an 710054, China
* Correspondence: ghxu@mail.xjtu.edu.cn

Abstract: The hand exoskeleton has been widely studied in the fields of hand rehabilitation and grasping assistance tasks. Current hand exoskeletons face challenges in combining a user-friendly design with a lightweight structure and accurate modeling of hand motion. In this study, we developed a finger exoskeleton with a rolling contact involute joint. Specific implementation methods were investigated, including an analysis of the mechanical characteristics of the involute joint model, the formula derivation of the joint parameter optimization algorithm, and the design process for a finger exoskeleton with an involute joint. Experiments were conducted using a finger exoskeleton prototype to evaluate the output trajectory and grasping force of the finger exoskeleton. An EMG-controlled hand exoskeleton was developed to verify the wearability and functionality of the glove. The experimental results show that the proposed involute joint can provide sufficient fingertip force (10N) while forming a lightweight exoskeleton to assist users with functional hand rehabilitation and grasping activities.

Keywords: mechanism design; rolling-contact joint; rehabilitation system

check for updates

Citation: Liang, R.; Xu, G.; Zhang, Q.; Jiang, K.; Li, M.; He, B. Design and Characterization of a Rolling-Contact Involute Joint and Its Applications in Finger Exoskeletons. *Machines* **2022**, *10*, 301. https://doi.org/10.3390/machines10050301

Academic Editor: Med Amine Laribi

Received: 22 March 2022
Accepted: 19 April 2022
Published: 24 April 2022

Publisher's Note: MDPI stays neutral with regard to jurisdictional claims in published maps and institutional affiliations.

Copyright: © 2022 by the authors. Licensee MDPI, Basel, Switzerland. This article is an open access article distributed under the terms and conditions of the Creative Commons Attribution (CC BY) license (https://creativecommons.org/licenses/by/4.0/).

1. Introduction

Hand exoskeletons represent a large portion of rehabilitation devices, as many of patients' interactions with the environment are performed via the hands [1]. According to the predictions of rehabilitation experts, by around 2024, people who suffer from hand dysfunction will be able to use portable exoskeletons to achieve basic daily activities in society, so the demand for portable hand exoskeletons will increase [2]. A series of hand exoskeletons has been developed thus far, and many of them are intended to assist people in daily life.

Soft robotics involves the study of how to make use of the softness of an object or a piece of material or system to build a robot that satisfies the softness level required by both its environment and its receiver [3]. The methods of soft exoskeleton robot implementation usually involve the use of compliant materials combined with pneumatic/hydraulic components as drivers [4–7], compliant control systems, such as the cable-driven system [8] or spring blade system [9] to control the gloves, or use topology optimization technology to optimize the mechanism configuration to guide the fingers [5,10]. These robots are usually lightweight and have a low profile. However, in some soft exoskeletons, such as tendon-based mechanisms, the applied forces may not be controlled accurately, thus resulting in a potential risk for the user.

Rigid-link structures facilitate the trajectories of human fingers through kinematic chains [11]. With an accurate trajectory and force directions, link-structure exoskeletons allow safe guidance for the finger [12–15]. However, linkage bars must be increased to achieve accurate motion fitting [1,16–18], which makes the structure of the exoskeleton.

Large-form factors and complex structures (especially when thumb opposition is assisted) are the major limitations of rigid-link exoskeletons.

When more motor functions are assigned to the exoskeleton, the mechanism is often complicated, which affects the wearing experience in terms of the human–computer interaction. However, when less motor function is assigned to the exoskeleton, movement guidance is not conducive to providing correct rehabilitation training. It can be concluded that designing a portable exoskeleton with motion-fitting ability and a compact structure has become a challenging problem in the field of hand exoskeletons.

In this study, we proposed a rolling contact involute joint for the design of a portable finger exoskeleton. First, we carried out the design of the involute joint and optimized the joint according to the motion generation ability. The involute joint was then applied to the design of the hand exoskeleton, and the kinematics and dynamics of the exoskeleton were verified by experiments.

The proposed involute joint was inspired by the most common grasping gesture of the human hand-the power grip. From an evolutionary perspective, the human hand has adapted to grasp cylindrical objects in their natural state, as the trajectory of the fingertip presents a circular involute-shaped curve in its relaxed state [19–24]. Compared with n-bar linkage exoskeletons, the proposed mechanism can provide a required output trajectory to fit the motion of human fingertips in an efficient way (fewer kinematic pairs) (Figure 1). The contributions of this study include the following:

(1) A rolling contact involute joint model was proposed, and we applied the joint as a motion-fitting solution for finger exoskeletons. When designing the involute finger exoskeleton, an optimization algorithm was introduced, and the driving position and spring mechanism were analyzed.
(2) A series of experiments was performed to measure the kinematic and dynamic properties of the finger exoskeleton. The results show that the proposed finger exoskeleton provides fingertip force with a maximum of 10 N, which is enough to support people in grasping daily heavy objects, such as a water bottle.
(3) We developed an EMG-controlled exoskeleton glove and conducted experimental verification of the exoskeleton. The wearability and functionality performance of the exoskeleton were verified.

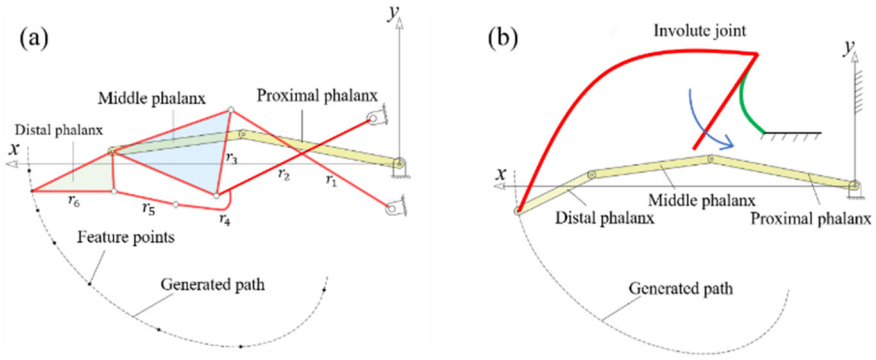


Figure 1. Comparison of the traditional linkage mechanism and the proposed joint model (Reprinted from [24]). (**a**) The n-bar linkage finger exoskeletons. (**b**) The proposed involute joint model.

The remainder of the article is organized as follows. Section 2 elaborates on the establishment of the proposed involute joint, presents an analysis of the optimization algorithm of the involute, and describes the mechanical design process of the finger exoskeleton, including the optimization of the driving positions, the spring systems, and the rolling contact mechanism. Section 3 presents the experiments conducted to test the motion fitting and force distribution of the finger exoskeleton prototype. Section 4 presents an EMG-controlled robotic hand exoskeleton. A motion intention recognition algorithm based on EMG was introduced, and the wearability and functionality performance of the exoskeleton were verified. Section 5 contains further discussion and conclusions.

2. Design of an Involute Rolling-Contact Finger Exoskeleton

2.1. Optimization of an Involute Joint for Path Generation

2.1.1. Kinematic Model of an Involute Joint

The motion of the rolling contact involute mechanism is the pure rolling of a plane (moving joint) around the corresponding surface (fixed joint). At every moment of joint movement, the plane l and the curve surface s are tangential to point C, which means that point C is always the instantaneous velocity center of plane l (Figure 2). When plane l rotates by angle θ, the positional relationship between the rotation center point and the output point can be described by Figure 2.

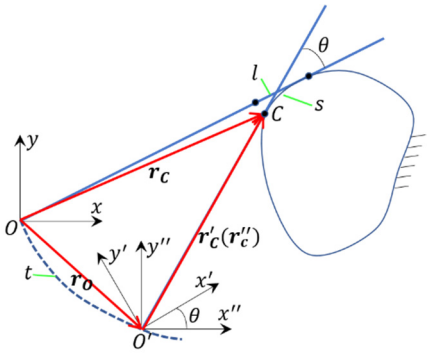


Figure 2. Kinematic analysis of the involute joint.

When plane l is rotated by angle θ, the position of the output point moves from point O to point O'. t represents the trajectory of the output point during the movement. The motion of plane l can be decomposed into the translation motion of the output point from a fixed coordinate system oxy into a translational coordinate system $o'x''y''$, and there is rotational motion around the output point (rotation from $o'x''y''$ to a rigid body coordinate system $o'x'y'$).

As shown in Figure 3, $\boldsymbol{r_c}$ and $\boldsymbol{r_o}$ represent the position vectors of C and O' in oxy, respectively. $\boldsymbol{r'_c}$ and $\boldsymbol{r''_c}$ represent the position vectors of C in the coordinate systems $o'x'y'$ and $o'x''y''$, respectively. The straight line (plane) l and the curve s represent the trajectories of the instantaneous velocity center C in oxy and $o'x'y'$, respectively. Thus, the relationship of vectors $\boldsymbol{r_o}$, $\boldsymbol{r_c}$, and $\boldsymbol{r''_c}$ can be expressed as

$$\boldsymbol{r_o} = \boldsymbol{r_c} - \boldsymbol{r''_c} \tag{1}$$

and as the vectors $\boldsymbol{r'_c}(x'_c, y'_c)$ and $\boldsymbol{r''_c}(x'_c, y'_c)$ are position vectors of C in $o'x'y'$ and $o'x''y''$,

$$\left.\begin{array}{l} x''_C = x\prime_C \cos\theta - y\prime_C \sin\theta \\ y''_C = x\prime_C \sin\theta + y\prime_C \cos\theta \end{array}\right\} \tag{2}$$

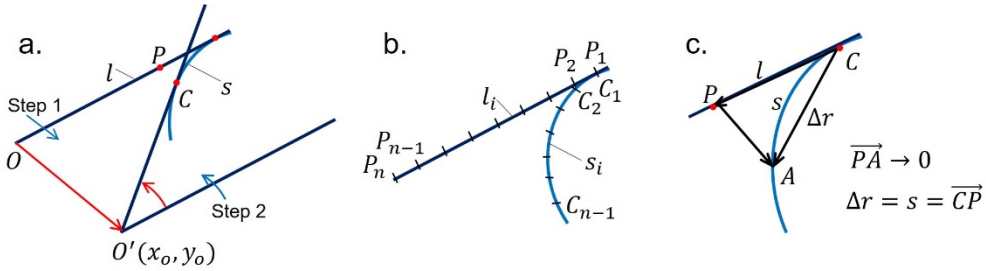


Figure 3. Discretization of pure rolling motion. (**a**) Plane motion of the rigid body with non-pure rolling. (**b**) Discretization of the pure rolling motion. (**c**) Differential analysis.

Formula (2) can be written as follows:

$$\boldsymbol{r}_{\boldsymbol{c}}'' = \boldsymbol{B}\boldsymbol{r}_{\boldsymbol{c}}' \tag{3}$$

where the following orthogonal displacement matrix $\boldsymbol{B}$ is

$$\boldsymbol{B} = \begin{pmatrix} \cos\theta & -\sin\theta \\ \sin\theta & \cos\theta \end{pmatrix} \tag{4}$$

By combining Equations (1) to (4), we obtain the following:

$$\left.\begin{array}{l} x'_C = (x_C - x_o)\cos\theta + (y_C - y_o)\sin\theta \\ y'_C = -(x_C - x_o)\sin\theta + (y_C - y_o)\cos\theta \end{array}\right\} \tag{5}$$

where x_o and y_o represent the positions of the output point after rotation.

Equation (5) describes the relationship between the position of point C on l and the position of point C on s before the rotation. When the rotation angle θ and the position of the output point O' are given, the position trajectories of the two contacting curves l and s can be determined. The kinematic analysis of the model reveals the factors that determine the output trajectory of the involute joint, which provides a valuable theoretical basis for the joint optimization algorithm.

2.1.2. Optimization of the Meshing Curve

In practical applications, the expected output path is composed of discrete desired points. The number of discrete points is determined by the measurement frequency. Equation (5) is derived from the position relation of the rigid body plane, which describes the position change of the rigid body plane before and after the motion. However, Equation (5) does not describe the contact relationship between two rigid bodies (i.e., pure rolling contact). In this case, any motion that satisfies Equation (5) is included. For example, as shown in Figure 3a, Equation (5) can also describe such a motion: plane l first moves in translation from oxy. When the output point reaches $O'(x_o,y_o)$, the plane rotates by an angle θ based on O'. The reason for the mismatch between the equation and the rolling-contact motion is that Equation (5) only describes the position relationship of the rigid body before and after the motion but does not describe the motion process. In other words, Equation (5) does not constrain l and s to be equal lengths.

In this paper, we discretize the curve s and the corresponding plane l, as shown in Figure 3b. The lengths of s and l can be calculated as follows:

$$L_s = \sum_{i=1}^{n} s_i, L_l = \sum_{i=1}^{n} \overrightarrow{P_{i-1}P_i} = \sum_{i=1}^{n} l_i \tag{6}$$

From the perspective of differentiation, when the discrete quantity n is large enough, the length of each curve length s_i will be equal to the corresponding line segment l_i ($s_i = \Delta r = l_i$), as shown in Figure 3c. In this way,

$$L_s = \sum_{i=1}^{n} s_i = \sum_{i=1}^{n} \overrightarrow{C_{i-1}C_i} = \sum_{i=1}^{n} \overrightarrow{P_{i-1}P_i} = L_l, (n \to +\infty) \tag{7}$$

To generate a suitable meshing involute joint, we propose an optimization method based on polylines from the perspective of geometric differentiation. The movement between plane l and surface s can be regarded as a fixed axis rotation in an instant. We use a polyline to replace curve s, and the straight line l is also divided into line segments. The shape of the polyline s is determined by the rotation center and rotation angle of each fixed-axis rotation; in other words, the lengths of s_i and θ_i in each rotation step determine the shape of the contact surface.

The goal of the optimization algorithm is to find the optimal positions of s_i and $\Delta\theta_i$ in each step. Figure 4 depicts the optimization iteration process of fixed-axis rotation in a single step.

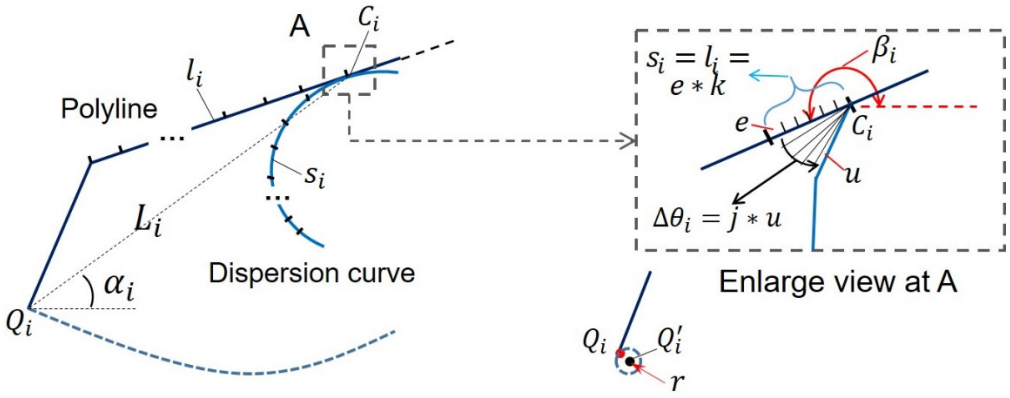


Figure 4. Discrete optimization process of the involute.

The first step of the optimization algorithm is to set up the threshold of the fitting precision, which is a threshold circle around the desired point Q'_i with a radius of r. When the values of $s_i(l_i)$ and $\Delta\theta_i$ are changed at each iteration of the loop, the position of the output point Q_i changes. When the output point Q_i is within the threshold circle, the optimization iteration of the current step ends, and the next optimization step starts.

For step i of the loop, $C_i(C_ix,C_iy)$ represents the rotating center of the multisegmented lines, and we assume that $C_i(C_ix,C_iy)$ is a known value. After a rotation of $\Delta\theta_i$, the output point Q_i reaches the threshold circle, the rotation stops, and the next rotating center $C_{i+1}(C_{i+1}x,C_{i+1}y)$ can be calculated as follows:

$$C_{i+1}x = s_i \cos(\beta_i + \Delta\theta_i) + C_ix \tag{8}$$

$$C_{i+1}y = s_i \sin(\beta_i + \Delta\theta_i) + C_iy \tag{9}$$

where s_i and θ_i are as follows:

$$s_i = ke, k = (1, 2, \ldots, m) \tag{10}$$

$$\Delta\theta_i = uj, j = (1, 2, \ldots, n) \tag{11}$$

where e is the step length, and m is the maximum number of iteration steps of s_i. Moreover, u is the iteration step size, and n is the maximum number of iteration steps of $\Delta\theta_i$. The azimuth of line l_i is as follows:

$$\beta_i = \beta_{i-1} + \Delta\theta_i \tag{12}$$

Through the double iterative of s_i and $\Delta\theta_i$, the position coordinates of the next output point Q_{i+1} in the threshold circle can be obtained:

$$Q_{i+1}x = L_i \cos\alpha_{i+1} + C_ix \tag{13}$$

$$Q_{i+1}y = L_i \sin(\alpha_i + \Delta\theta_i) + C_iy \tag{14}$$

where L_i represents the rotating radius of the output point in step i of the iteration.

$$L_i = \sqrt{(C_ix - Q_ix)^2 + (C_iy - Q_iy)^2} \tag{15}$$

The angle in the parametric equation can thus be expressed as follows:

$$\alpha_{i+1} = \alpha_i + \Delta\theta_i \tag{16}$$

When the position of the output point Q_{i+1} is within the threshold circle of point Q'_{i+1}, which is

$$\text{dist}|Q_{i+1}, Q\prime_{i+1}| \leq r \tag{17}$$

the program steps out of the ith iteration.

Once the s_i and $\Delta\theta_i$ values in each optimization step have been obtained, the shape of the polyline is drawn. Accordingly, the meshing point in straight line l can be calculated as follows:

$$P_{i+1}x = \text{dist}|C_{i+1}x, C_ix| \cos\beta_1 + P_ix \tag{18}$$

$$P_{i+1}y = \text{dist}|C_{i+1}y, C_iy| \sin\beta_1 + P_iy \tag{19}$$

where $P_1 = C_1$.

In this way, by calculating the positions of C_i and P_i, a pair of rolling contact joints for the desired output point is obtained, and point Q_i is the actual output position of the joint.

2.1.3. Design of an Involute Joint for an End-Effect Finger Device

We applied the proposed rolling-contact involute joint to the design of a finger exoskeleton. A motion capture system (VICON) was adopted to measure the motion of the index finger (Figure 5). VICON includes ten T40 MX cameras (three other cameras are not shown in the photograph) that measure the motion of the markers at a frequency of 100 fps.

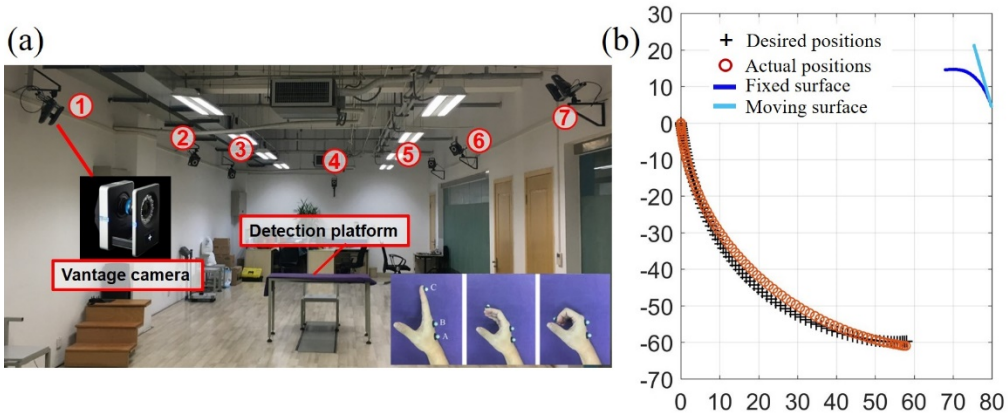


Figure 5. Design of an Involute Joint for the End-effect Finger. (**a**) Motion capture of the fingertip. (**b**) Optimization results for the involute joint.

Three hand postures-flexion, relaxation, and extension—were introduced in [25]. As shown in Figure 5, the subject relaxed his fingers from the flexion posture and moved the fingers to the extended position with minimal force. By using the natural contraction of the fingers with minimal force, the potential for idiosyncratic motions was minimized. General postures can be applied to the grasping of everyday objects, such as cups, small balls, etc. Hence, we captured the trajectory of the subject's fingertip in these general postures.

We combined the captured fingertip trajectory and used the proposed optimization algorithm to design the involute joint. The initial values of the algorithm included the initial rotation radius L_1, threshold radius r, optimal step sizes of e and u, and two position angles α_1 and β_1. Table 1 shows the initial values of the optimization loop.

Table 1. Initial values of the optimization loop.

Initial Values	Threshold Radius (mm)	Rotation Radius (mm)	Step Size of $\Delta\theta_i$ (mm)	Step Size of s_i (rad)	Initial Position (rad)	Initial Angle (rad)
Symbol	r	$L(1)$	U	e	α_1	β_1
Value	2	80	0.001	0.005	$56\pi/55$	$7\pi/12$

Figure 5 presents the trajectory of the fingertip obtained from the experiment, which includes 80 positional data items of the marker. The black dots Q_i in the figure are the positions of the subject's fingertip captured by VICON. The red circles represent the optimized output positions of the involute joint. The magenta and blue curves are two contacting curves that consist of 80 scattered points. The correlation coefficient of the calculated output positions according to the desired positions was 0.97.

2.2. Optimization of the Driving Position and Spring Mechanism

2.2.1. Optimization of the Driving Position

The plane diagram of the involute finger exoskeleton is shown in Figure 6. We used a linear motor to drive the finger exoskeleton. As different positions of the motor led to various driving trajectories and driving distances, we optimized the driving position according to the driving distance of the motor.

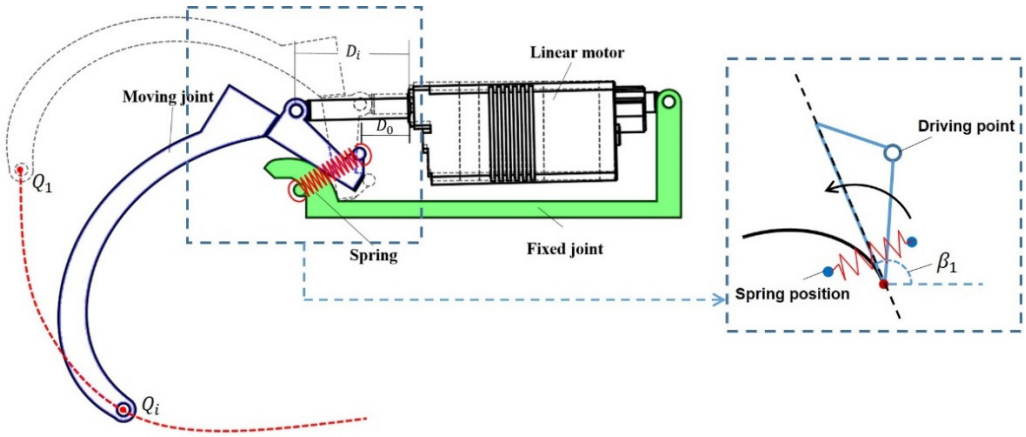


Figure 6. Diagram of the involute finger exoskeleton.

As the linear motor began to drive from its initial position, the involute plane rotated around the curve surface. The movement and workspace of the linear motor depended on the initial position of the driving point. To observe the movement of driving points at different positions when the joint rotated, we selected three driving points at different positions for motion simulation. The initial position angle of the linear motor was set to be $\alpha = 0$, $\pi/6$, or $\pi/3$, as shown in Figure 7. The maximum distance of the driving position, which is the length between the initial and final positions of the driving trajectory, is shown in the figure.

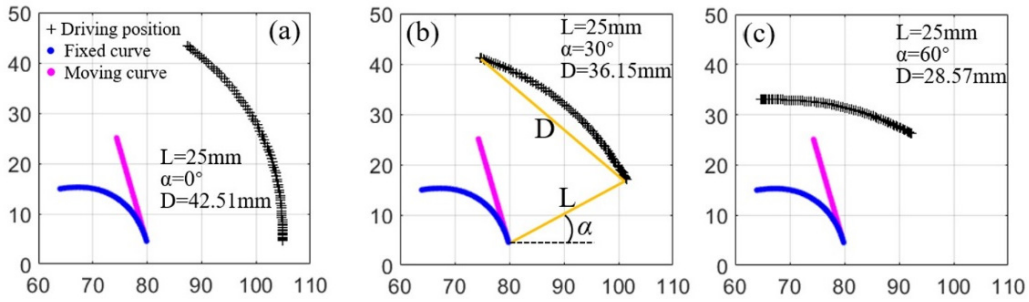


Figure 7. Three driving points at different positions for motion simulation. The initial position angles of α, (**a**) 0, (**b**) $\pi/6$, and (**c**) $\pi/3$.

In Figure 7, $D = \text{dist}\,|\,D_1, D_n\,|$, where D_1 represents the first driving position, and D_n represents the final driving position. In this study, since the number of desired positions measured was 80, the value of n was 80. The position length of the driving point was set to be L = 25 mm, and the driving point produced a variety of trajectories according to the position angle α.

To select the appropriate driving point, we needed to calculate the maximum driving distance when the driving point was located in different positions. We set up a rectangular design domain ($Lx \times Ly$) near the initial meshing point and divided the design domain into $n = (nx + 1) \times (ny + 1)$ grids (Figure 8a). Each node in the grid represented a new position of the driving point $D_{i,j}$, for $i,j = (1,2, \ldots, N)$. When $D_{i,j}$ was at a new position, the trajectory of the driving point was drawn, and the maximum driving distance was calculated. Correspondingly, to show the driving distance in the design domain, we set a grid of $(nx + 1) \times (ny + 1)$, as shown in Figure 8b. We drew the contour map according to the maximum driving distance of each position (Figure 9) so that the designer was able to select the appropriate driving point position according to the stroke of the motor. Each element in the grid represents the actual driving distance (D) at the current position.

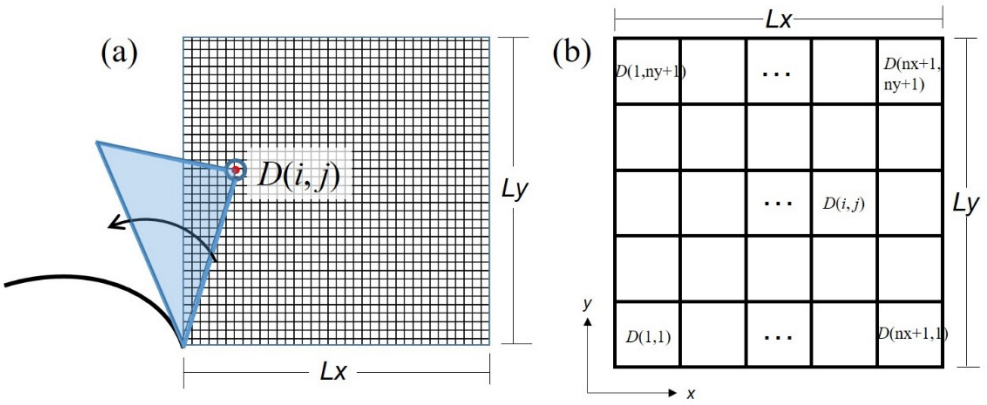


Figure 8. Distribution of the maximum driving distance (D). (**a**) Rectangular design domain ($Lx \times Ly$). (**b**) Meshing of the design domain.

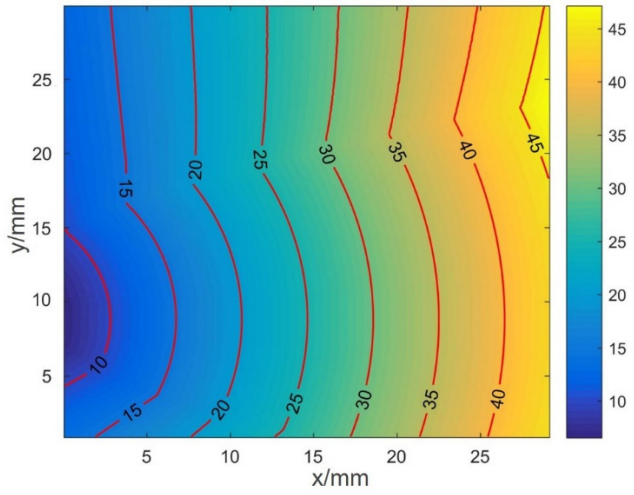


Figure 9. Contour map of the maximum driving distance.

Here, we used a linear motor with a stroke of 30 mm to drive the joint, which required the maximum drive distance to be less than 30 mm. According to the contour map of D, the suitable driving position for this design is located on the left side of the 30 mm contour. We selected position $D_{i,j}$ (x = 3.06 mm, y = 24.8 mm) as the driving point.

After selecting the driving position of the motor, the trajectory of the driving point was drawn, and the velocity of the output point was also determined. As shown in Figure 10, when the driving point of the motor was at position D_i, the driving velocity vector along the linear motor was $\boldsymbol{v_{Di}}$. Meanwhile, the moving plane Π attached to the moving joint rotated around the contact point M_i. The actual velocity vector of point D_i was $\boldsymbol{v_{Mi}}$, perpendicular to D_iM_i. Thus, it was possible to obtain the angular velocity ω_{Mi} of the moving plane Π

by calculating the velocity vector v_{Mi}. This then allowed the velocity vector of the output point v_{Qi} to be calculated. The relationships among the variables were as follows:

$$|\omega_{Mi}| = \frac{\left|\overrightarrow{v_{Di}}\right| \cos(\varphi_i)}{dist|D_iM_i|} \tag{20}$$

where φ_i represents the angle between the velocity vector at point Di and the velocity vector of the linear motor. Following the calculation of the angular velocity of the rigid body plane, the velocity vector of the fingertip output point Qi on the plane can be expressed as follows:

$$\left|\overrightarrow{v_{Qi}}\right| = |\omega_{Mi}|dist|M_iQ_i| \tag{21}$$

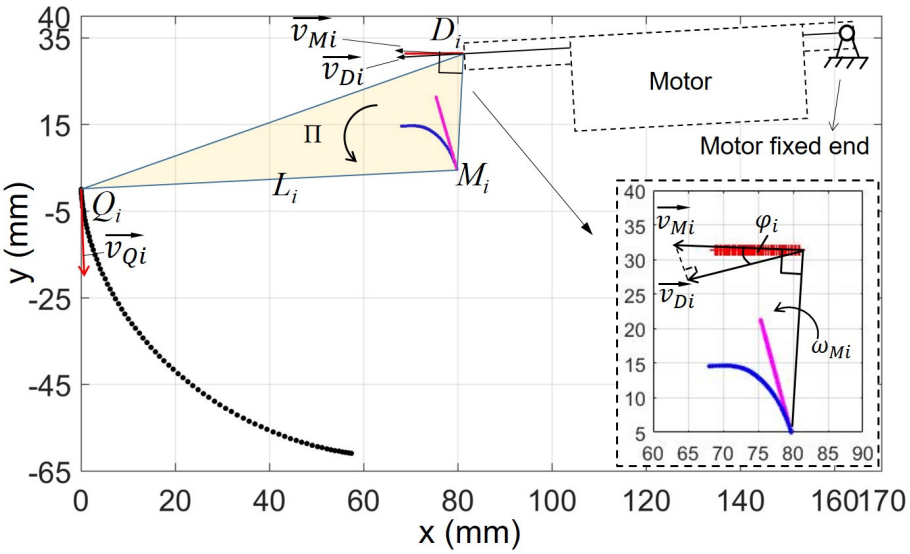


Figure 10. Relationship between the driving velocity and the output velocity.

The direction of the velocity vector in position Q_i is the tangential direction of the fingertip trajectory, that is, perpendicular to *DiMi*.

In this way, when the velocity of the linear motor is known, the velocity vector at the fingertip can be obtained. The uniform linear motor used in this study had a speed of about 10 mm/s. We obtained an output velocity variation diagram of the moving joint at the characteristic positions, as shown in Figure 11a. It can be seen from the figure that the output speed of the moving joint at the fingertip continued to increase as the bending angle increased. Accordingly, we drew output velocity vector diagrams for different positions, as shown in Figure 11b.

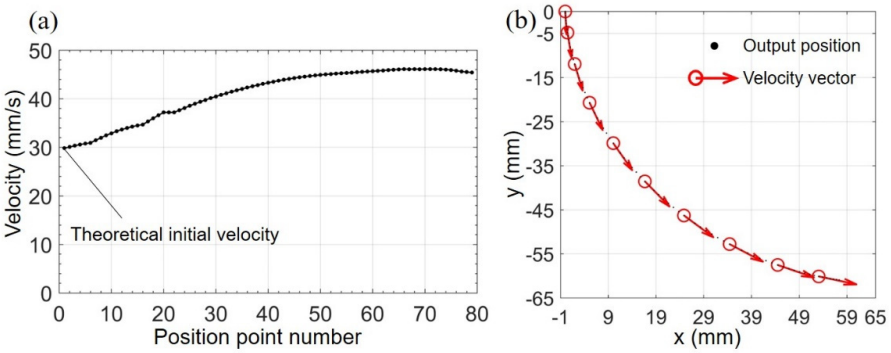


Figure 11. Output velocity of the moving joint. (**a**) Variation in the output velocity of the moving joint at the feature points. (**b**) Velocity vector diagram.

2.2.2. Spring Mechanism

A spring system was installed to connect the plane and the curve surface. The spring force acted as resistance when the exoskeleton joint rotated, providing sufficient contact pressure for the two contacting surfaces. The spring was stretched when the motor actuated the moving joint (the plane) to rotate. In Figure 12, point A represents the fixed mounting point of the spring, while point B is the movable mounting point. As the moving joint rotated around the fixed joint, point B showed a specific trajectory (Figure 12). Therefore, elastic force was generated in the extending direction, acting as a passive impedance. The guiding force was calculated by spring deflection. For a specific assembling spring, the spring force is determined only by its spring stiffness k, as described in (22). Figure 13 shows the variation tendency of the spring force (that is, the elongation of the spring).

$$F_i = (L_i - L_1)k, (i = 1, 2, \ldots, n) \tag{22}$$

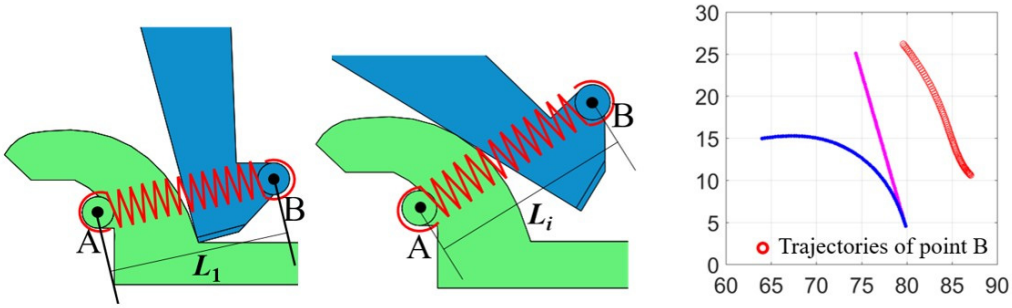


Figure 12. Trajectory of the spring mounting point.

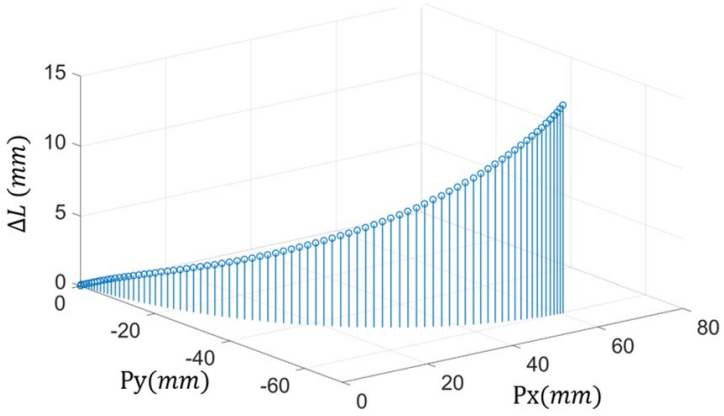


Figure 13. Variation tendency of the spring force.

The projection of the scatter on the X-Y plane represents the trajectory of the output point Q_i. From the figure, it can be observed that the spring force continued to increase nonlinearly during the flexion of the joint.

2.2.3. Rolling Contact Design of Involute Surfaces

As the joint rotated, the plane of the moving joint pressed against the curved surface of the fixed joint. Here, we used steel straps to connect the two components (the plane and the curve surface), which formed a restraint system that allowed the two components to roll in relation to another contact surface without a slip. Figure 14 shows the structure of the steel strap design. As shown in the figure, three steel straps were used in the design. The ends of each steel strap were fixed on the moving joint and the fixed joint, respectively. The rolling contact design could help to achieve greater stability and ensure pure rolling of the joint during rotation. Compared with the hybrid cam-linkage exoskeleton in [26], the

rolling contact design presented a compact and simple structure, and the joint generated relatively little friction.

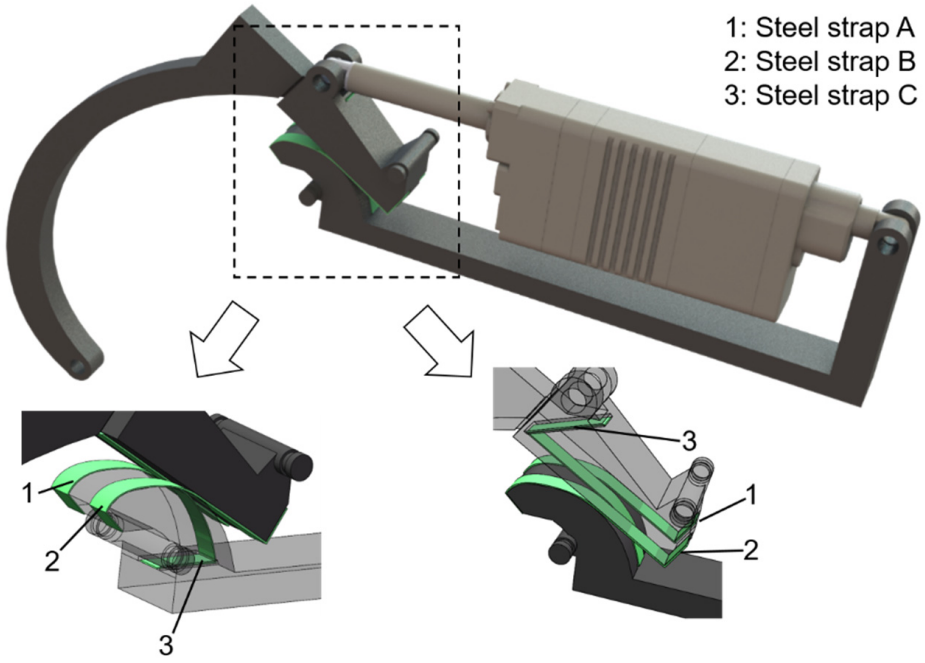


Figure 14. Rolling contact design of the involute surfaces.

3. Performance Verification

We constructed a prototype for exercising index finger extension and flexion. The exoskeleton was fabricated using a 3D printer, and the structure of the device was designed to be compact and lightweight. Velcro was added to the wearing part, providing a comfortable wearable experience for the subject. In this section, we demonstrate tests of the kinematic and dynamic properties of the joint.

3.1. Output Trajectory of the Exoskeleton

We verified the output trajectory of the finger exoskeleton system. The finger exoskeleton was worn on the subject's finger for motion performance verification. Markers A, B, and C were attached to the output point of the prototype, and VICON was used to track the movement. Marker A represents the actual output point of the prototype. The output trajectory of the exoskeleton was measured 10 times, and the obtained data were compared with the desired fingertip trajectory (Figure 15). The blue line shows the polynomial curve that was fitted to the experimental data. The equation for the fitted polynomial was as follows:

$$y = p_1x^4 + p_2x^3 + p_3x^2 + p_4x + p_5 \tag{23}$$

where $p_1 = 9.024 \times 10^{-6}$, $p_2 = -0.001464$, $p_3 = 0.09705$, $p_4 = -3.523$, and $p_5 = 0.3679$.

The experimental results of the output trajectory of the mechanism match well with the actual fingertip trajectory. Minor deviations in the experimental results were caused by dimensional tolerances associated with the 3D fabrication process, gap errors between rotation surfaces, errors caused by wearing, and errors of motion capture.

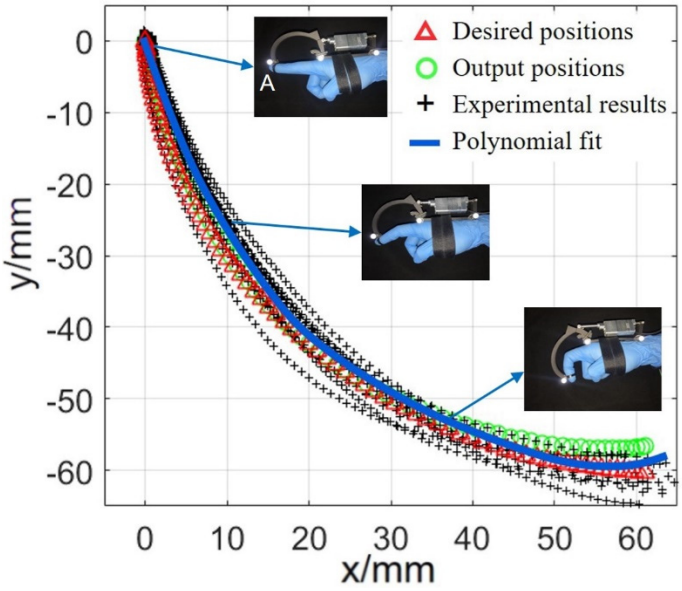


Figure 15. Motion performance verification of the exoskeleton.

3.2. Performance of the Free-Space Simulation

The influence of the spring on fingertip force is important, as it demonstrates the antagonistic resistance of the exoskeleton. A six-axis sensor (ATI Nano17, ATI Inc., Apex, NC, USA) was used to test the dynamic performance of the exoskeleton. The sensor was bound to the fingertip using Velcro. A customized finger cap was manufactured to mount a six-axis force/torque sensor beneath the fingertip. The fixed end of the force/torque sensor was fixed to the finger cap. We disassembled the motor from the exoskeleton. The user moved his finger at a nearly constant velocity back and forth four times. Furthermore, the resistant force of the fingertip was measured. The maximum force was approximately 1.3 N, as shown in Figure 16.

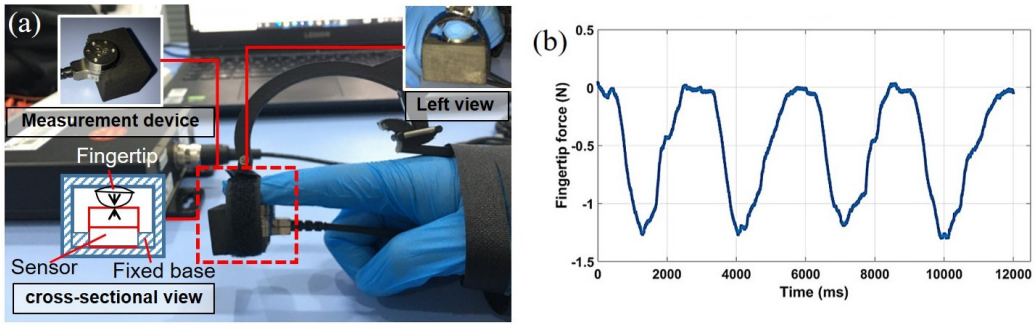


Figure 16. Fingertip force in free-space flexion. (**a**) The principle of the measurement device. (**b**) Fingertip force.

3.3. Performance of the Grasping Simulation

Here, we tested the exoskeleton's ability to grasp a cylinder. The measurement system is shown in Figure 17. A cylindrical cup with an outside diameter of 70 mm was fabricated using a 3D printer, and a six-axis force/torque sensor (ATI Nano17, ATI Inc., USA) was installed in the cup. The grasping performance was tested as the finger exoskeleton drove the finger to grasp the cup. As the motor was driven, the index finger began to contact the sensor in the cup. During the grasping process, we increased the output force by increasing the stroke of the motor. When the fingertip force reached about 10 N, the coupler showed no obvious deformation.

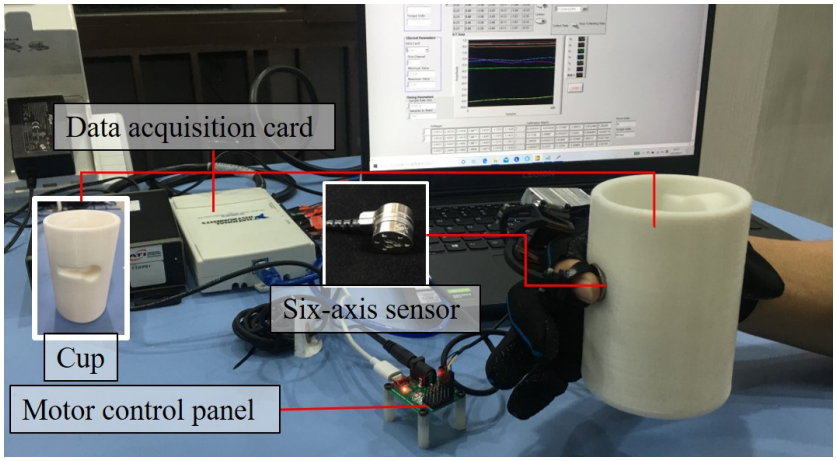


Figure 17. Experiment for grasping simulation.

The contact force on the cup was measured using the sensor. Figure 18 shows the variation in the grasping force on the cup when the user grasped the cup back and forth twice. The results demonstrate that the finger exoskeleton provided a considerable force for the finger to grasp objects. In [9], it was proven that a fingertip force of 6.4 n is sufficient to lift heavy objects, such as a 500 mL bottle.

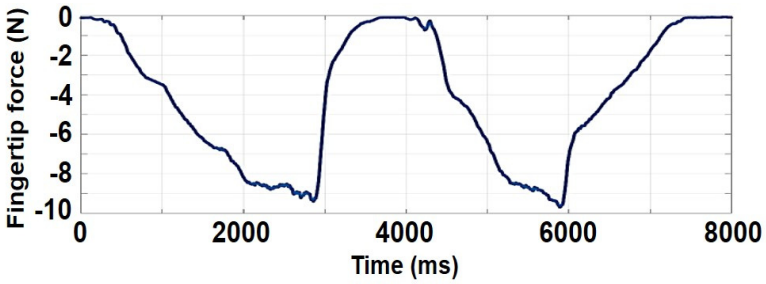


Figure 18. Grasping force of the fingertip.

4. An EMG-Controlled Robotic Hand Rehabilitation System

4.1. Design Implementation

To verify the function of the proposed involute joint, we designed a training system based on EMG control (Figure 19). The design of the system focused on lowering the weight and volume, improving the convenience of wearing, and arranging the motors, battery, and electronics appropriately. Five finger exoskeletons were mounted on a customized glove using Velcro tape. The lithium battery and controller were installed in a 3D printing electronic module box and tied to the arm. The Myo-Armband (Thalmic Labs, ON, Canada) was worn on the user's healthy arm. In this way, the user was able to control the arm on the dysfunctional side through the arm on the healthy side for rehabilitation training.

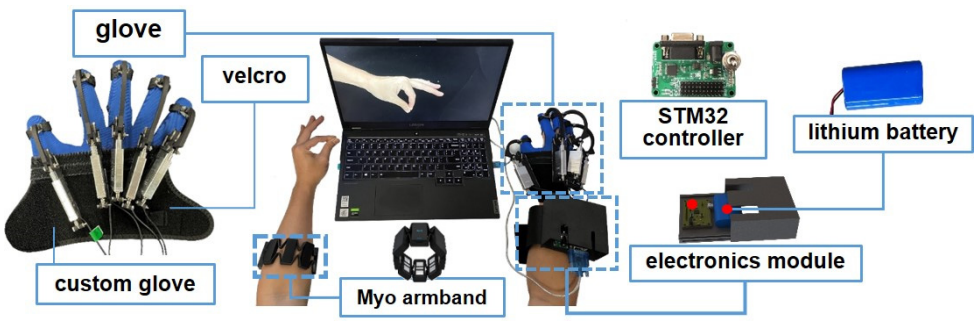


Figure 19. EMG-Controlled Robotic Hand Rehabilitation System.

Figure 20 shows a block diagram of the system. The Myo Armband is connected to a computer through Bluetooth communication. The Myo-Armband position includes eight pairs of dry electrodes to capture muscular activity. After receiving EMG signals from the Myo-Armband, the host computer converts the analyzed motion intention into the control command of the exoskeleton and sends it to the STM32 controller, which controls the motor to realize the corresponding motion of the glove.

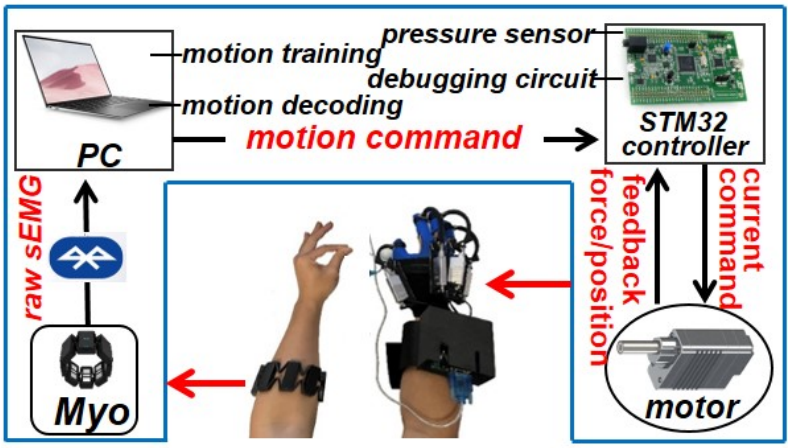


Figure 20. Block diagram of the system.

4.2. Motion Intention Detection

The intention detection function of the EMG signals must have high recognition accuracy for different hand gestures and for the same hand movement but by different users. We calculated the RMS amplitude of the EMG signal and compared it with the RMS amplitude of the EMG signal in the resting state so that the initiation time of the hand movement could be identified in real time. After recognizing the hand movement intention, we decomposed the characteristic matrix of the myoelectric signal to obtain the muscle cooperative structure so as to identify the hand posture. The hand pose recognition algorithm used was as follows:

First, we represented the multiple EMG signals as a linear combination model of multiple muscles:

$$V_{N,S} = W_{N,R} \times H_{R,S} \tag{24}$$

where $V_{N,S}$ is the matrixes of the time series, which represent the EMG signal characteristics of N channels; each column in $W_{N,R}$ represents a mode of muscle group synergy; and each row in $H_{R,S}$ represents the activation coefficient corresponding to the muscle group synergy in $W_{N,R}$.

Second, we decomposed the characteristic matrix of the training samples to obtain a standardized $W_{N,R}$. We then used the non-negative matrix factorization (NMF) algorithm to solve the muscle cooperation model and obtain $H_{R,S}$ for each training sample.

Finally, the $H_{R,S}$ obtained from the training samples was used as the classification feature, and a support vector machine (SVM) classifier was used to classify the collected EMG signals. In this way, we were able to compare the user's muscle group cooperation mode with the training sample database to determine the user's movement intention.

To verify the effectiveness of the intention recognition algorithm, we designed four basic gestures and carried out sample training. The gestures included Extension, Flexion, Palmar pinch, and Medium wrap. The subjects were told to carry out hand-movement training according to the training gestures on the computer screen. EMG signals from the eight channels of Myo were recorded, and Features were computed within a sliding window of 200 ms. Figure 21a compares the original training data for subject S1 with the results after dimensionality reduction with NMF. We set the number of base vectors R in the base vector matrix W to 4. After the optimal set of features had been selected, the information content from the 8 Myo channels was calculated. Subject S1 was told to repeat

the four gestures 10 times, and the Myo information from the training was recorded. The information for each channel was displayed by norm normalization, as shown in Figure 21b. The Myo content for Hand extension and Hand flexion was more informative than that for Palmar pinch and Medium wrap. The information in channel 1 (C1) had a high weight (74%) for Hand extension. For the two movements of Palmar pinch and Medium wrap, the Myo data in S1 showed a certain degree of discreteness. For Palmar pinch, the data collected by C2 had a high level of discreteness (24–51%).

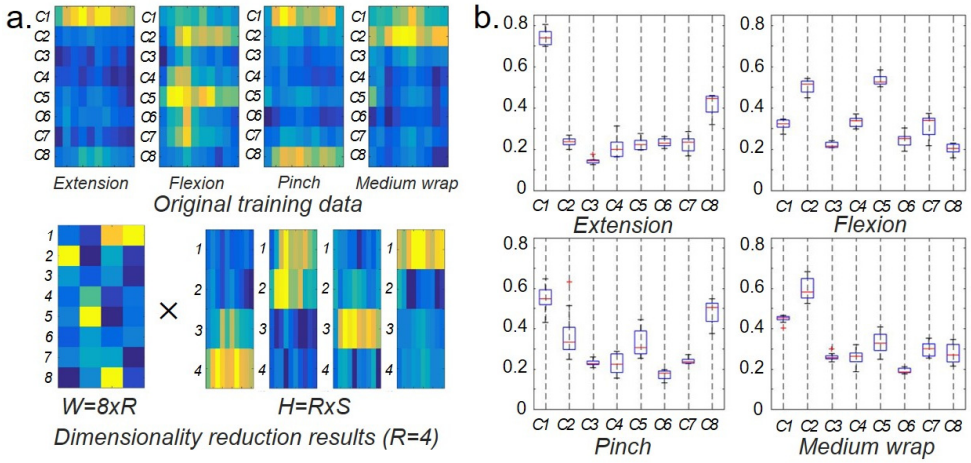


Figure 21. Functional verification of training system. (**a**) Dimension reduction analysis of Myo EMG signal. (**b**) Distribution characteristics of the training data for the four gestures.

4.3. Wearability and Functionality Testing

The exoskeleton verification experiment included wearability and functionality tests. The wearability testing verified the independent donning and doffing of a glove with a single hand via a wearability evaluation. The functionality test verified the accuracy of the intention recognition algorithm.

There were ten participants in the experiment (8 males and 2 females, aged 23–31). First, subjects were asked to put on the glove with a single hand. The steps of donning were divided into (**1**) the Myo armband and (**2**) the exoskeleton glove and electronics module. On the contrary, the steps of doffing were divided into (**1**) the electronics module and (**2**) the Myo armband. Then, we recorded the time taken to don and doff the glove. The donning/doffing time started once the subject touched the Myo armband/electronics module and stopped when he/she released it. Two trials of fully donning and doffing the glove were completed. Table 2 reports the average time taken to don and doff the glove recorded in the two trials. During the trials, the participants were asked not to rush, and the subjects had a simple training trial before timing. The wearability evaluation gave a promising result, showing that all participants were able to don and doff the training system with a single hand independently after a simple practice trial.

Table 2. Donning and doffing times.

Wearing Step	Donning(s)		Doffing(s)	
	1st Trial	2nd Trial	1st Trial	2nd Trial
1	7.74	5.96	4.89	5.35
2	30.06	31.35	9.47	8.57

To test the functionality of the training system, ten subjects were tested for motion recognition. Each subject was told to perform four trained movements with their left hand, with each movement performed 10 times. Every time the subject made a gesture with their left hand, we checked whether the glove worn to drive the right hand made the same movement. Finally, we recorded the judgment results for all gestures made by all subjects.

A receiver operating characteristic curve (ROC) was drawn to evaluate the performance of the intention recognition algorithm. Sensitivity (*or the true positive rate* on the vertical axis) measures the proportion of correctly identified events from the total number of samples, which is

$$Sensitivity = \frac{TP}{TP + FN} \tag{25}$$

where TP, FN, and FP are the true positives, false negatives, and false positives, respectively.

Figure 22 shows the sensitivity of the functionality testing results. The figure shows the true positive vs. false positive rate calculated over all trials performed by each subject. For each gesture, the true positive rate was above 0.9, and the false positive rate was below 0.05.

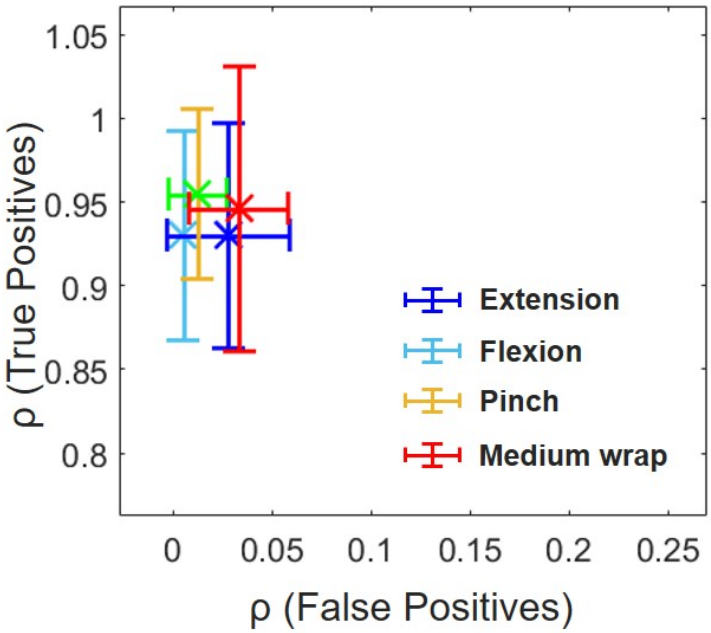


Figure 22. Detection results for the true positive vs. the false positive rate.

5. Discussion and Conclusions

The experimental results show that the proposed involute joint provides proper motion guidance for the fingers, as well as a certain active force for the fingertips. The rolling contact solution is the key technology for the proposed involute joint. In this study, we present the design of the involute of an arbitrary curve for the joint, rather than the circular involute. In solving the problem of curve fitting, the involute of an arbitrary curve has a better fitting effect than the involute of a normal circle. The advantages of the rolling-contact design in the finger exoskeleton joint are as follows: on the one hand, compared with soft hand devices, it can provide the desired trajectory precisely for the fingertip, and on the other hand, its joint structure remains simple compared with the linkage exoskeletons, which ensures that the exoskeleton is lightweight. In this paper, we used black nylon (Young's modulus: 1.7GPa) for the fabrication of the exoskeleton. The current version of the glove is light (362 g), while the fingertip force (10N) is in the range of other state-of-the-art rigid exoskeletons. Table 3 compares the proposed exoskeleton and other advanced devices. The proposed rolling-contact involute exoskeleton has a relatively low mass (376.5 g, including the actuators) and can drive five fingers independently with a large fingertip force (10 N).

Table 3. Comparison of the proposed exoskeleton with other advanced devices.

Hand Exoskeleton	Weight (g)	Finger Number	Fingertip Force (N)	Actuation Method
Involute joint exoskeleton	175 (without actuator) 376.5 (with actuator)	5	10	Linear motor
FLEXotendon Glove-II [27]	n/a	3	5.03	DC motor (cable driven)
RELab tenoexo [9]	148 (without actuator) 788 (with actuator)	5	6.4	DC motor (cable driven + spring blade)
Exo-Glove [28]	194 (without actuator)	3	12	DC motor (cable driven)
Force-feedback glove [26]	245 (without actuator)	5	4	Pneumatic pump
Evan et al. [29]	700 (without actuator)	5	n/a	Linear motor
Thumb-Exoskeleton [17]	n/a	5	3.11	DC motor
Rigid-soft exoskeleton [30]	95 (without actuator) 324 (with actuator)	5	6	Linear motor
Mano [31]	50 (without actuator) 930 (with actuator)	5	5	cable driven
ExoGlove [32]	200 (without actuator)	5	3.59	Pneumatic pump
Fabric-Based Actuators [33]	78.6 (without actuator)	5	n/a	Pneumatic pump
Enfolded-Textile Actuator [34]	160 (without actuator)	5	n/a	Pneumatic pump

At present, the proposed involute joint is a single-degree-of-freedom joint, which can realize patients' daily grasping movements. For multitrajectory grasping, a diversified meshing surface design may be involved. In addition, a suitable dynamic model may be helpful for comprehensively analyzing the mechanical properties of involute joints. We will further analyze the dynamic properties of joints in future research.

The proposed glove exoskeleton has advantages in terms of weight and wearability and can be compatible with other intention detection systems (see the Myo-armband in Section 4). At this stage, our most important task is to apply the glove to clinical trials. Through clinical trials on patients, more functional requirements and defects of gloves will be found, which will help us to make further improvements.

In this study, we proposed a rolling contact involute joint and developed a compact EMG-controlled exoskeleton system. A trajectory optimization algorithm was proposed for the design of the involute joint. The kinematic and dynamic characteristics of the finger exoskeleton were tested. We also conducted functionality and wearability tests to verify the performance of the EMG-controlled glove. In future work, we aim to further optimize the rolling-contact involute joint to achieve a multitrajectory function. We also plan to add distributed tactile feedback to the user's fingertip to provide the sensation of contact with objects. The involute joint model may be applied to other human joint exoskeletons, such as the elbow and knee joints. The application of the proposed involute joints to other human joints (such as the *elbow* and *knee* joints) is also worthy of further research. Finally, since increasing the flexibility of joints can improve the wearability of an exoskeleton, we plan to carry out an integrated flexible design of involute joints in combination with the use of 3D printing technology in the future.

Author Contributions: Made substantial contributions to the research and investigation process, reviewed and summarized the literature, wrote and edited the original draft, R.L.; Performed oversight and leadership responsibilities for research activity planning and execution, as well as developed ideas and the evolution of the overarching research aims, G.X., K.J. and Q.Z. carried out the lab experiments; Performed a critical review, commentary and revision, M.L.; Provided technical, and material support, B.H. All authors have read and agreed to the published version of the manuscript.

Funding: This research was funded by the Science and Technology Plan Project of Xi'an, (Grant No. 20KYPT0001-10) and Key projects in Shaanxi Province (Grant No. 2021GXLH-Z-008), and the Xi'an Key Laboratory of Brain Computer Interaction & Neuroregulation Digital Medicine.

Institutional Review Board Statement: The study was conducted in accordance with the Declaration of Helsinki, and approved by the Institutional Review Board (or Ethics Committee) of Xi'an Jiaotong University (protocol code:2021-1430. date of approval: 5 July 2021).

Informed Consent Statement: Informed consent was obtained from all subjects involved in the study.

Data Availability Statement: Not applicable.

Conflicts of Interest: The authors declare no conflict of interest.

References

1. Jones, C.L.; Wang, F.; Morrison, R.; Sarkar, N.; Kamper, D.G. Design and Development of the Cable Actuated Finger Exoskeleton for Hand Rehabilitation Following Stroke. *IEEE/ASME Trans. Mechatron.* **2014**, *19*, 131–140. [CrossRef] [PubMed]
2. Ferris, D.P. The exoskeletons are here. *J. Neuroeng. Rehabil.* **2009**, *6*, 17. [CrossRef] [PubMed]
3. Chen, A.; Yin, R.; Cao, L.; Yuan, C.; Ding, H.; Zhang, W. Soft robotics: Definition and research issues. In Proceedings of the 2017 24th International Conference on Mechatronics and Machine Vision in Practice (M2VIP), Auckland, New Zealand, 21–23 November 2017; IEEE: Piscataway, NJ, USA, 2017; pp. 366–370.
4. Li, H.; Cheng, L.; Li, Z.; Xue, W. Active Disturbance Rejection Control for a Fluid-Driven Hand Rehabilitation Device. *IEEE/ASME Trans. Mechatron.* **2020**, *26*, 841–853. [CrossRef]
5. Zhang, H.; Kumar, A.S.; Chen, F.; Fuh, J.Y.H.; Wang, M.Y. Topology Optimized Multimaterial Soft Fingers for Applications on Grippers, Rehabilitation, and Artificial Hands. *IEEE/ASME Trans. Mechatronics* **2019**, *24*, 120–131. [CrossRef]
6. Yap, H.K.; Khin, P.M.; Koh, T.H.; Sun, Y.; Liang, X.; Lim, J.H.; Yeow, C.H. A fully fabric-based bidirectional soft robotic glove for assistance and rehabilitation of hand impaired patients. *IEEE Robot. Autom. Lett.* **2017**, *2*, 1383–1390. [CrossRef]
7. Li, C.; Gu, X.; Ren, H. A Cable-Driven Flexible Robotic Grasper With Lego-Like Modular and Reconfigurable Joints. *IEEE/ASME Trans. Mechatron.* **2017**, *22*, 2757–2767. [CrossRef]
8. Sun, N.; Li, G.; Cheng, L. Design and Validation of a Self-Aligning Index Finger Exoskeleton for Post-Stroke Rehabilitation. *IEEE Trans. Neural Syst. Rehabil. Eng.* **2021**, *29*, 1513–1523. [CrossRef]
9. Bützer, T.; Lambercy, O.; Arata, J.; Gassert, R. Fully Wearable Actuated Soft Exoskeleton for Grasping Assistance in Everyday Activities. *Soft Robot.* **2021**, *8*, 128–143. [CrossRef]
10. Zheng, Y.; Cao, L.; Qian, Z.; Chen, A.; Zhang, W. Topology optimization of a fully compliant prosthetic finger: Design and testing. In Proceedings of the 2016 6th IEEE International Conference on Biomedical Robotics and Biomechatronics, Singapore, 26–29 June 2016; IEEE: Piscataway, NJ, USA, 2016; pp. 1029–1034.
11. Bos, R.A.; Haarman, C.J.; Stortelder, T.; Nizamis, K.; Herder, J.L.; Stienen, A.H.; Plettenburg, D.H. A structured overview of trends and technologies used in dynamic hand orthoses. *J. Neuroeng. Rehabil.* **2016**, *13*, 1–25. [CrossRef]
12. Lu, Z.; Tong, R.K.-Y.; Zhang, X.; Li, S.; Zhou, P. Myoelectric Pattern Recognition for Controlling a Robotic Hand: A Feasibility Study in Stroke. *IEEE Trans. Biomed. Eng.* **2018**, *66*, 365–372. [CrossRef]
13. Esposito, D.; Centracchio, J.; Andreozzi, E.; Savino, S.; Gargiulo, G.D.; Naik, G.R.; Bifulco, P. Design of a 3D-Printed Hand Exoskeleton Based on Force-Myography Control for Assistance and Rehabilitation. *Machines* **2022**, *10*, 57. [CrossRef]
14. Orlando, M.F.; Behera, L.; Dutta, A.; Saxena, A. Optimal Design and Redundancy Resolution of a Novel Robotic Two-Fingered Exoskeleton. *IEEE Trans. Med. Robot. Bionics* **2020**, *2*, 59–75. [CrossRef]
15. Secciani, N.; Bianchi, M.; Ridolfi, A.; Volpe, F.V.Y.; Governi, L.; Bianchini, M.; Allotta, B. Tailor-Made Hand Exoskeletons at the University of Florence: From Kinematics to Mechatronic Design. *Machines* **2019**, *7*, 22. [CrossRef]
16. Fontana, M.; Dettori, A.; Salsedo, F.; Bergamasco, M. Mechanical design of a novel Hand Exoskeleton for accurate force displaying. In Proceedings of the 2009 IEEE International Conference on Robotics and Automation, Kobe, Japan, 12–17 May 2009. [CrossRef]
17. Gabardi, M.; Solazzi, M.; Leonardis, D.; Frisoli, A. Design and Evaluation of a Novel 5 DoF Underactuated Thumb-Exoskeleton. *IEEE Robot. Autom. Lett.* **2018**, *3*, 2322–2329. [CrossRef]
18. Leonardis, D.; Barsotti, M.; Loconsole, C.; Solazzi, M.; Troncossi, M.; Mazzotti, C.; Castelli, V.P.; Procopio, C.; Lamola, G.; Chisari, C.; et al. An EMG-Controlled Robotic Hand Exoskeleton for Bilateral Rehabilitation. *IEEE Trans. Haptics* **2015**, *8*, 140–151. [CrossRef] [PubMed]
19. Linde-Medina, M. Adaptation or exaptation? The case of the human hand. *J. Biosci.* **2011**, *36*, 575–585. [CrossRef]
20. Kamper, D.G.; Cruz, E.G.; Siegel, M.P. Stereotypical fingertip trajectories during grasp. *J. Neurophysiol.* **2003**, *90*, 3702–3710. [CrossRef]
21. Borghesan, G.; Palli, G.; Melchiorri, C. Design of tendon-driven robotic fingers: Modeling and control issues. In Proceedings of the 2010 IEEE International Conference on Robotics and Automation, Anchorage, AK, USA, 3–7 May 2010; IEEE: Piscataway, NJ, USA, 2010; pp. 793–798.
22. Omarkulov, N.; Telegenov, K.; Zeinullin, M.; Begalinova, A.; Shintemirov, A. Design and analysis of an underactuated anthropomorphic finger for upper limb prosthetics. In Proceedings of the 2015 37th Annual International Conference of the IEEE Engineering in Medicine and Biology Society (EMBC), Milan, Italy, 25–29 August 2015; IEEE: Piscataway, NJ, USA, 2015; Volume 2015, pp. 2474–2477.

23. Kang, L.; Seo, J.T.; Kim, S.H.; Kim, W.J.; Yi, B.J. Design and implementation of a multi-function gripper for grasping general objects. *Appl. Sci.* **2019**, *9*, 5266. [CrossRef]
24. Liang, R.; Xu, G.; Teng, Z.; Li, M.; Zhang, S.; Zheng, X.; Zhang, K.; He, B. A General Arthropod Joint Model and its Applications in Modeling Human Robotic Joints. *IEEE Access* **2021**, *9*, 7814–7822. [CrossRef]
25. Neumann, D.A. *Kinesiology of the Musculoskeletal System-e-Book: Foundations for Rehabilitation*; Elsevier Health Sciences: Amsterdam, The Netherlands, 2016.
26. Zheng, Y.; Wang, D.; Wang, Z.; Zhang, Y.; Zhang, Y.; Xu, W. Design of a Lightweight Force-Feedback Glove with a Large Workspace. *Engineering* **2018**, *4*, 869–880. [CrossRef]
27. Tran, P.; Jeong, S.; Wolf, S.L.; Desai, J.P. Patient-Specific, Voice-Controlled, Robotic FLEXotendon Glove-II System for Spinal Cord Injury. *IEEE Robot. Autom. Lett.* **2020**, *5*, 898–905. [CrossRef]
28. Chang, P.H.; Lee, S.H.; Koo, K.M.; Lee, S.H.; Jin, S.H.; Yeo, S.S.; Seo, J.P.; Jang, S.H. The cortical activation pattern by a rehabilitation robotic hand: A functional NIRS study. *Front. Hum. Neurosci.* **2014**, *8*, 49. [CrossRef] [PubMed]
29. Susanto, E.A.; Tong, R.K.; Ockenfeld, C.; Ho, N.S. Efficacy of robot-assisted fingers training in chronic stroke survivors: A pilot randomized-controlled trial. *J. Neuroeng. Rehabil.* **2015**, *12*, 1–9. [CrossRef] [PubMed]
30. Liang, R.; Xu, G.; Li, M.; He, B.; Khalique, U. Fusing Topology Optimization and Pseudo-Rigid-Body Method For the Development of a Finger Exoskeleton. *IEEE Robot. Autom. Lett.* **2021**, *7*, 1721–1728. [CrossRef]
31. Randazzo, L.; Iturrate, I.; Perdikis, S.; Millan, J.D.R. mano: A Wearable Hand Exoskeleton for Activities of Daily Living and Neurorehabilitation. *IEEE Robot. Autom. Lett.* **2018**, *3*, 500–507. [CrossRef]
32. Yap, H.K.; Lim, J.H.; Nasrallah, F.; Goh, J.C.; Yeow, R.C. A soft exoskeleton for hand assistive and rehabilitation application using pneumatic actuators with variable stiffness. In Proceedings of the 2015 IEEE International Conference on Robotics and Automation (ICRA), Seattle, WA, USA, 26–30 May 2015; pp. 4967–4972.
33. Cappello, L.; Galloway, K.C.; Sanan, S.; Wagner, D.A.; Granberry, R.; Engelhardt, S.; Haufe, F.L.; Peisner, J.D.; Walsh, C.J. Exploiting Textile Mechanical Anisotropy for Fabric-Based Pneumatic Actuators. *Soft Robot.* **2018**, *5*, 662–674. [CrossRef]
34. Nassour, J.; Hamker, F.H.; Cheng, G. High-Performance Perpendicularly-Enfolded-Textile Actuators for Soft Wearable Robots: Design and Realization. *IEEE Trans. Med Robot. Bionics* **2020**, *2*, 309–319. [CrossRef]